Materials Science in Semiconductor Processing 216 (2026) 111081

Contents lists available at ScienceDirect

Materials Science in Semiconductor Processing

journal homepage: www.elsevier.com/locate/mssp

Deep-defect suppression in Sb_2Se_3 via atmosphere-dependent selenization probed by photoluminescence spectroscopy

N. Abbasi *, J. Krustok, R. Kaupmees, K. Timmo, V. Mikli, M. Kauk-Kuusik, M. Grossberg-Kuusk

Department of Materials and Environmental Technology, Tallinn University of Technology, Ehitajate tee 5, Tallinn, 19086, Estonia

ARTICLE INFO

Keywords:
Sb_2Se_3
Selenization
Photoluminescence
Deep defects
Excitons

ABSTRACT

The recombination dynamics in Sb_2Se_3 are strongly governed by intrinsic defect states, which limit carrier lifetime and solar cell device performance. In this work, the influence of post-growth selenization under controlled vapor pressure conditions on defect-related recombination in Sb_2Se_3 polycrystals is investigated using temperature- and excitation power-dependent photoluminescence (PL) spectroscopy. Structural characterization confirms preservation of the orthorhombic phase after selenization, while Raman analysis indicates improved crystallinity, particularly for the sample selenized under an argon atmosphere. The as-grown polycrystals exhibit four emission bands at 0.88 eV, 1.10 eV, 1.22 eV, and 1.29 eV, corresponding to recombination via deep localized defect states (0.88 eV), grain-boundary-related states (1.10 eV), donor-acceptor pair (DAP) (1.22 eV), and excitonic (1.29 eV) recombination, respectively. Upon selenization, the grain-boundary-related and donor–acceptor pair recombination bands are suppressed, while the deep-level emission is significantly reduced but remains present, and excitonic emission becomes dominant. Excitation power-dependent measurements further confirm the distinction between defect-related and excitonic recombination mechanisms. Overall, the results demonstrate that increasing vapor pressure during selenization effectively suppresses radiative recombination via defect states and enhances excitonic edge emission, identifying vapor pressure as a key parameter controlling defect-mediated radiative recombination in Sb_2Se_3.

1. Introduction

The development of stable inorganic thin-film photovoltaic devices with well-controlled processing conditions remains an important challenge in solar energy research. Widely used thin-film absorber materials, such as CdTe and $Cu(In,Ga)Se_2$, are typically polycrystalline and therefore contain grain boundaries that introduce recombination-active states, degrading device performance. Addressing these defects often requires additional processing steps, such as defect passivation or high-quality crystal growth, which increase fabrication complexity and cost [1,2].

In this context, antimony selenide Sb_2Se_3, with its quasi-one-dimensional (Q1D) ribbon-like crystal structure, offers a promising alternative for ultrathin photovoltaic applications, as its anisotropic bonding and reduced density of dangling bonds at surfaces limit defect-related recombination and enable efficient carrier transport even at reduced thicknesses [3]. Sb_2Se_3 has emerged as a promising absorber material due to its nearly-optimal band gap of 1.1–1.3 eV for solar energy conversion [4] and its optical absorption in the visible region ($>10^5\ cm^{-1}$), enabling efficient light harvesting even in thin absorber layers [5]. In addition, its simple binary composition, based on earth-abundant elements, and its single-phase orthorhombic crystal structure make it attractive for scalable and cost-effective device fabrication [6]. Carrier lifetimes in Sb_2Se_3 span multiple timescales depending on the experimental technique employed. Ultrafast methods reveal picosecond-scale carrier relaxation (~20-40 ps) [7], while time-resolved photoluminescence (PL) measurements show recombination lifetimes shorter than 1 ns (~0.1-0.6 ns) [8], and transient absorption studies report carrier decay on the nanosecond scale (~4 ns) [9]. This broad range of timescales reflects the complexity of the defect structure and recombination processes in Sb_2Se_3. As a result, although device efficiencies approaching 11% have been reported, a substantial open-circuit voltage (V_{OC}) deficit compared to theoretical limits persists [10].

* Corresponding author.
E-mail address: nafiseh.abbasi@taltech.ee (N. Abbasi).

https://doi.org/10.1016/j.mssp.2026.111081
Received 25 May 2026; Received in revised form 5 August 2026; Accepted 11 August 2026
Available online 13 August 2026

The V_{OC} deficit is primarily attributed to intrinsic point defects and their complex defect chemistry. Although Sb_2Se_3 is a binary compound, its low-symmetry Q1D ribbon-like structure, $[Sb_4Se_6]_n$, in which weak van der Waals interactions connect ribbons, gives rise to multiple crystallographically non-equivalent atomic sites with distinct coordination environments [11]. For instance, selenium vacancies may form at several inequivalent lattice positions, commonly denoted as V_{Se1}, V_{Se2}, and V_{Se3}, each associated with unique local bonding configurations and defect levels. As a result, defect formation becomes highly site-dependent, leading to a wide variety of intrinsic defects, including antisites (Sb_{Se} and Se_{Sb}), interstitials (Sb_i and Se_i), and vacancies (V_{Se} and V_{Sb}). Consequently, Sb_2Se_3 exhibits a significantly more complex defect landscape than typical binary semiconductors, with deep-level states that strongly influence recombination dynamics and device performance [12].

First-principles DFT calculations further reveal that defect formation strongly depends on the selenium chemical potential. Under Se-rich conditions, low-formation-energy acceptor-type antisite defects (Se_{Sb} and $2Se_{Sb}$) are favored, promoting *p*-type conductivity. Conversely, Se-poor conditions favor donor-type defects, which introduce deep levels within the band gap and act as efficient recombination centers, thereby reducing carrier lifetimes and V_{OC} [11].

Experimental studies support these findings. Deep-level transient spectroscopy studies have identified intrinsic electron traps located between ~0.35 and 0.7 eV below the conduction band in both bulk single crystals and thin films, confirming their intrinsic point defect origin rather than grain boundary effects [13]. Although Se-rich growth conditions can suppress deep selenium vacancies such as V_{Se1} and V_{Se3}, non-stoichiometry leads to the formation of deep defects, and the deep donor V_{Se2} defect (located ~0.3 eV below the conduction band at T = 300 K) remains energetically stable and intrinsically limits device efficiency [6,14]. These findings emphasize the critical role of selenium chemical potential in governing defect formation and recombination processes in Sb_2Se_3.

Significant improvements in absorber quality can be attained through advanced deposition techniques [5,10], controlled doping [15], and post-deposition thermal treatments [16–20]. In particular, selenization has been widely used to enhance structural and optoelectronic properties by promoting recrystallization and compensating for selenium loss during deposition [16,21–23]. Previous studies, such as that of Uslu et al. [24], demonstrated that selenization under controlled argon pressure improves grain orientation and film compactness, leading to enhanced current density and device performance through improved structural quality. Similarly, controlled Se diffusion has been reported to improve film quality by reducing void formation, optimizing grain orientation, and modifying the $MoSe_2$ interfacial layer, resulting in enhanced device performance [22]. However, these improvements have been evaluated primarily through structural and device-level characterization, without providing direct insight into defect-related recombination processes.

While several PL studies have identified recombination mechanisms in Sb_2Se_3, most have focused on intrinsic defect characterization or doping effects, and the influence of post-growth processing conditions, particularly annealing atmosphere, on defect-related recombination has not been systematically explored [25–27].

PL has been applied to investigate recombination processes in Sb_2Se_3. Grossberg et al. [26] reported three PL bands at T = 10 K located at 0.94 eV, 1.10 eV, and 1.24 eV. The emissions at 0.94 eV and 1.24 eV were attributed to deep donor-deep acceptor pairs (DD-DA) recombination and donor–acceptor pair (DAP) recombination, respectively, while the band at 1.10 eV was associated with grain-boundary-related recombination. Temperature-dependent measurements yielded activation energies of approximately 93 meV, 65 meV, and 33 meV for the respective PL bands. The excitation power dependence of the integrated PL intensity of all three bands followed the sublinear dependence with a power coefficient of k ~0.6, indicating recombination of charge carriers localized at defect states within the band gap. In addition to defect-related emission, band-edge recombination has been investigated by Krustok et al. [25], who identified free exciton and biexciton emissions in the energy range 1.31–1.33 eV in Sb_2Se_3 microcrystals at T = 3 K. The excitation-power dependence of the PL intensity showed k = 1 for free excitons and k = 2 for biexcitons, while the temperature dependence of these PL bands followed the band gap variation, consistent with band-edge recombination. The role of defects in recombination has been further clarified through comparative studies of undoped and doped Sb_2Se_3. In a PL study at T = 8 K, Abbasi et al. [27] observed two emission bands in the undoped crystal at 0.89 eV and 1.02 eV, while the Cl-doped crystal exhibited bands at 0.84 eV and 1.09 eV. The higher-energy band at 1.09 eV was attributed to DD–DA recombination with an activation energy of approximately 42 meV. The lower-energy band at 0.84 eV exhibited negative thermal quenching that was explained by a recombination model involving a deep acceptor and a Cl-induced shallow donor, likely associated with a Cl_{Se} antisite defect. These results demonstrate that both intrinsic defects and extrinsic dopants define the recombination pathways in Sb_2Se_3.

In this work, PL spectroscopy is employed as a powerful, non-destructive tool to investigate how post-growth selenization under different atmospheric conditions influences intrinsic recombination channels in Sb_2Se_3. By comparing PL signatures, we demonstrate that argon-assisted selenization can suppress specific deep-level emissions, providing direct spectroscopic evidence for atmosphere-dependent defect passivation.

2. Experimental

Sb_2Se_3 polycrystals were synthesized from elemental Sb and Se (99.999%, Alfa Aesar) precursors, which were handled in a glove box under an inert atmosphere to prevent oxidation. The precursors were weighed according to the stoichiometric Sb_2Se_3 composition, thoroughly mixed, and milled in an agate mortar to obtain a homogeneous powder. The resulting precursor mixture was loaded into a quartz ampoule, which was subsequently degassed and vacuum-sealed. Solid-state synthesis was carried out in a single-zone chamber furnace using a stepwise heating profile. The temperature was increased to 200 °C over 3 h and held for 24 h, followed by a further increase to 550 °C over 3 h and a dwell time of 300 h to promote crystal growth.

The maximum synthesis temperature (550 °C) was chosen to remain below the melting point of Sb_2Se_3 (~590-610 °C) [28,29], thereby avoiding melt-induced phase segregation while enabling sufficient atomic diffusion for crystallization. The stepwise heating profile facilitates initial Sb and Se reactions at lower temperatures prior to high-temperature crystal growth, while the prolonged annealing ensures complete reaction and high crystallinity. After the synthesis and crystallization process, the ampoule was removed from the furnace and allowed to cool to room temperature in ambient air.

For post-treatment, three quartz ampoules ($d = 1$ cm; $l = 32.5$ cm; $V = \sim 25\ cm^3$) were prepared, with 0.2 g Sb_2Se_3 placed at one end of each ampoule and an elemental Se pellet introduced at the other end. After evacuation, two ampoules were sealed under vacuum (vac), while one additional ampoule was backfilled with argon to 200 Torr at room temperature before sealing (Ar200). The presence of argon was used to regulate Se vapor transport and suppress excessive Se vapor accumulation during high-temperature annealing.

The treatments were carried out for 1 h in a two-temperature zone furnace, with the Sb_2Se_3 source maintained at 500 °C and the Se source at either 415 °C or 440 °C, corresponding to a Se vapor pressure of ~5 Torr and ~10 Torr, respectively, in vacuum-sealed ampoules. To further increase the effective vapor pressure, the argon-filled ampoule was annealed with the Sb_2Se_3 source maintained at 500 °C and the Se pellet at 440 °C, resulting in a total pressure of approximately 488 Torr. This post-treatment resulted in three distinct conditions combining vac and Ar200 at each Se pressure. These pressure conditions were selected

based on previous optimization of the selenization process. The investigated samples are hereafter referred to as as-grown, Se-5, Se-10, and Se + Ar-488, corresponding to increasing vapor pressure conditions during selenization. Schematic selenization steps are depicted in Fig. 1.

The microstructure of Sb_2Se_3 powder crystals was investigated by a high-resolution scanning electron microscope (SEM) Zeiss Ultra 55. The elemental composition of the polycrystals was determined by Energy Dispersive X-ray Spectroscopy (EDX) using a Bruker Esprit 1.8 system on a Zeiss Merlin high-resolution Scanning Electron Microscope (HR-SEM). For the SEM images, the microscope was operated at 15 kV in secondary-electron mode (SE2 detector). The crystal structure of the polycrystalline samples was analyzed by X-ray diffraction (XRD) using a Rigaku Ultima IV diffractometer with Cu Kα radiation ($\lambda = 1.5406$ Å) operated at 40 kV and 40 mA. Diffraction patterns were collected in θ–2θ geometry over the 2θ range 10–70° with a step width of 0.02° in continuous scan mode, using a D/teX Ultra silicon strip detector and a Kβ filter. The average crystallite sizes and lattice strain were determined using the Halder–Wagner method [30] as implemented in the PDXL software, based on the reflections of the orthorhombic Sb_2Se_3 phase. The phase analysis was performed using room-temperature micro-Raman analysis with Horiba's LabRam HR800 spectrometer with a 532 nm line of the YAG: Nd laser.

For the PL measurements, the polycrystals were mounted on the cold finger of a closed-cycle helium cryostat (Janis CCS-150, Lake Shore Cryotronics), and measurements were carried out in the temperature range of 8–300 K. The temperature was controlled using a Lake Shore Model 335 temperature controller. A pulsed CryLaS FQSS266-Q2 laser ($\lambda = 532$ nm) with a maximum average power of $P_{max} = 7.5$ mW, peak energy of 1.1 μJ, pulse width <1 ns, and repetition frequency of 10 kHz was employed as the excitation source. The emitted PL was dispersed by a single-grating monochromator (Horiba) and detected using a Hamamatsu InGaAs photodetector. The PL signal was selectively enhanced using a lock-in amplifier, enabling the separation from the background noise. Neutral density filters were used to vary the incident laser power density, which was adjusted in the range of 15–1500 mW/cm^2. The presented PL spectra were not corrected for the spectral response of the detector. Note that the band-edge emission of Sb_2Se_3 (~1.30 eV ≈ 955 nm) lies at the short-wavelength edge of the InGaAs detector sensitivity range, where the responsivity decreases steeply toward higher photon energies.

3. Results and discussion

3.1. Structural properties

SEM images revealed that the synthesized Sb_2Se_3 consists of well-developed microcrystalline grains, indicating significant grain growth during the prolonged high-temperature annealing process. Although the material remains polycrystalline, the large grains suggest substantial crystallization during synthesis. No noticeable changes in morphology are observed after vacuum or argon post-treatment (Fig. 2). EDX point analyses (8 measurements per sample) confirmed near-stoichiometric compositions for all samples, with average atomic concentrations of Sb ~ 40 at.% and Se ~ 60 at.% (Table 1). Nevertheless, a slight increase in Se content is consistently observed in vacuum- and argon-treated samples, in agreement with the expected effect of selenization. While the overall grain morphology with characteristic layered growth features is preserved after the Se-5 and Se-10 post-treatments (Fig. 2b and c), the Se + Ar-488 sample exhibits a noticeably smoother surface with less pronounced layered features (Fig. 2d), indicating enhanced surface recrystallization under the highest vapor pressure conditions; since the annealing temperature (500 °C) remains well below the melting point of Sb_2Se_3, this modification is limited to the surface, as confirmed by the unchanged EDX composition, XRD patterns, and Raman spectra.

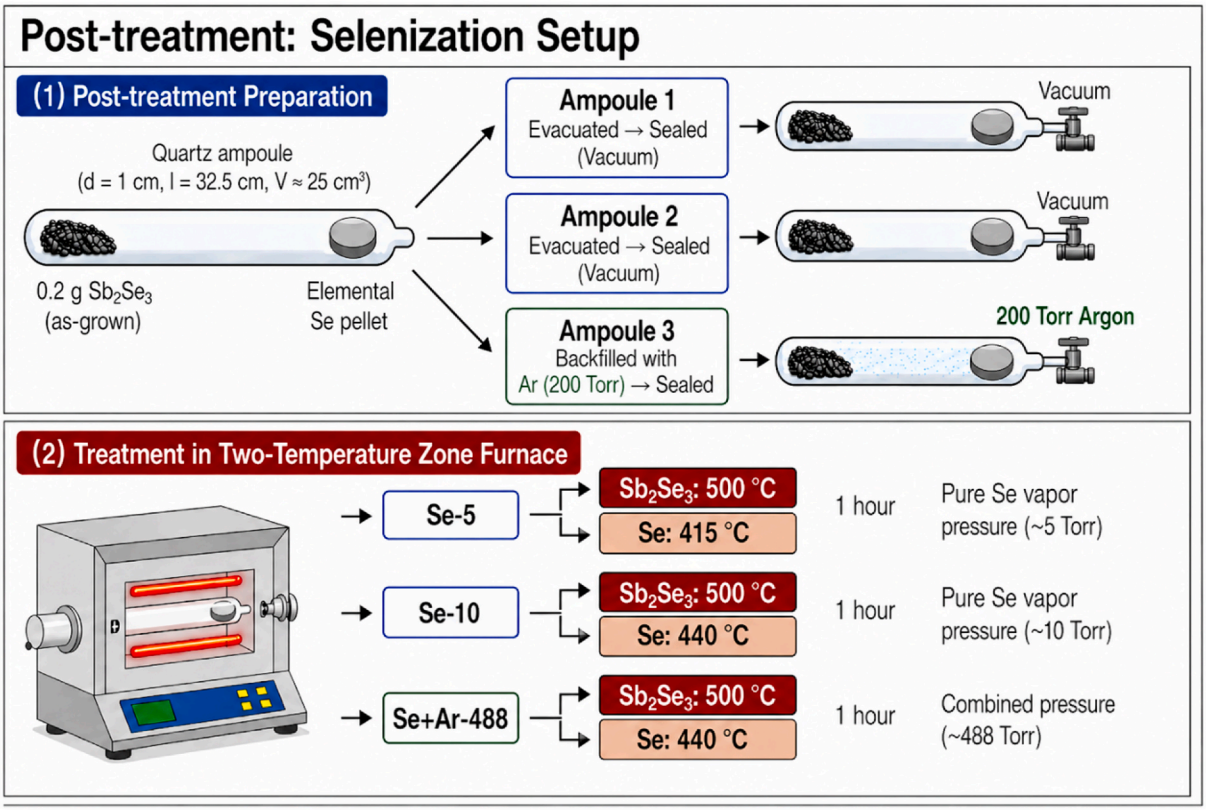

Fig. 1. Schematic illustration of post-growth selenization process in a two-zone furnace using sealed quartz ampoules. Each ampoule contained Sb_2Se_3 powder and elemental Se placed at opposite ends. The Sb_2Se_3 zone was maintained at 500 °C, while the Se zone was set to either 415 °C or 440 °C. The ampoules were sealed either under vacuum or with Ar (200 Torr), resulting in three distinct post-treatment conditions.

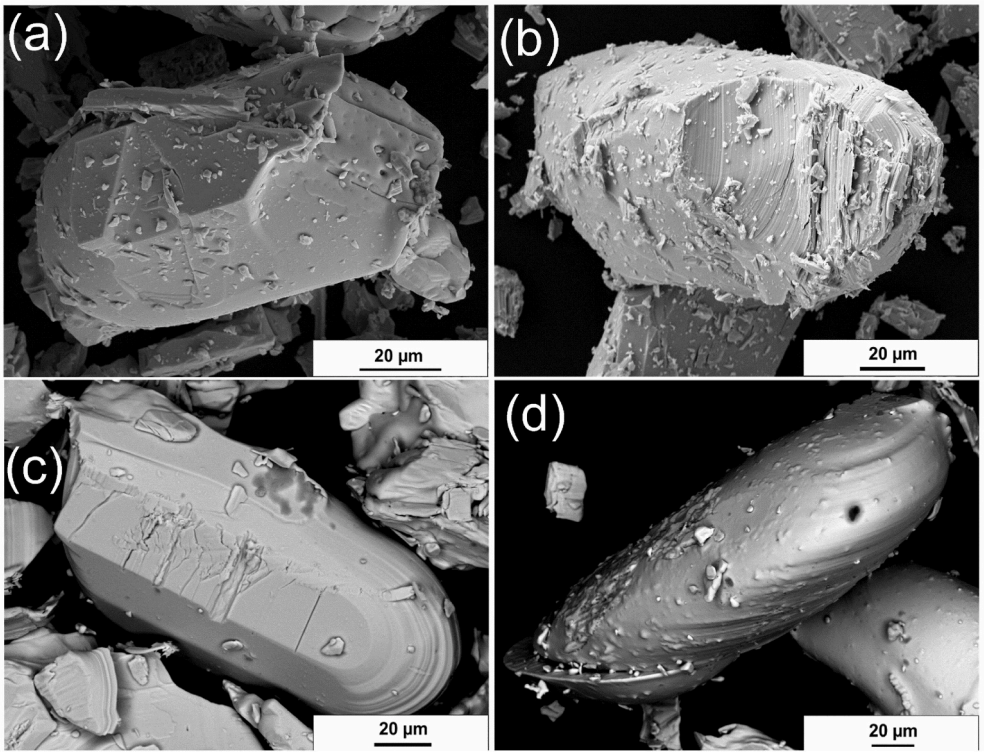

Fig. 2. Scanning electron microscope images of Sb_2Se_3 samples, showing well-developed microcrystalline grain morphology for (a) as-grown, (b) Se-5, (c) Se-10, and (d) Se + Ar-488.

Table 1
Average elemental composition of as-grown and post-treated Sb_2Se_3 polycrystals obtained by EDX (8 measurements per sample).

Sample name	Sb (at.%)	Se (at.%)	Sb/Se Atomic Ratio
as-grown	40.9	59.1	0.69
Se-5	40.3	59.7	0.67
Se-10	40.2	59.8	0.67
Se + Ar-488	40.3	59.7	0.67

XRD patterns of the as-grown and post-treated Sb_2Se_3 polycrystals (Fig. 3a) confirmed the formation of orthorhombic Sb_2Se_3 (space group *Pnma*), consistent with ICDD reference data. The diffraction patterns exhibit the characteristic reflections at 2θ ~15°, 17°, 28°, 31°, and 34°.

The lattice parameters obtained from pattern refinement are *a* ~1.180 nm, *b* ~0.399 nm, and *c* ~1.165 nm, in good agreement with reported values for orthorhombic Sb_2Se_3 [31]. No significant changes in the diffraction patterns or lattice parameters are observed after post-treatments, indicating preservation of the crystal structure and confirming Sb_2Se_3 as the dominant crystalline phase in all samples. To quantify the structural changes upon selenization, the average crystallite

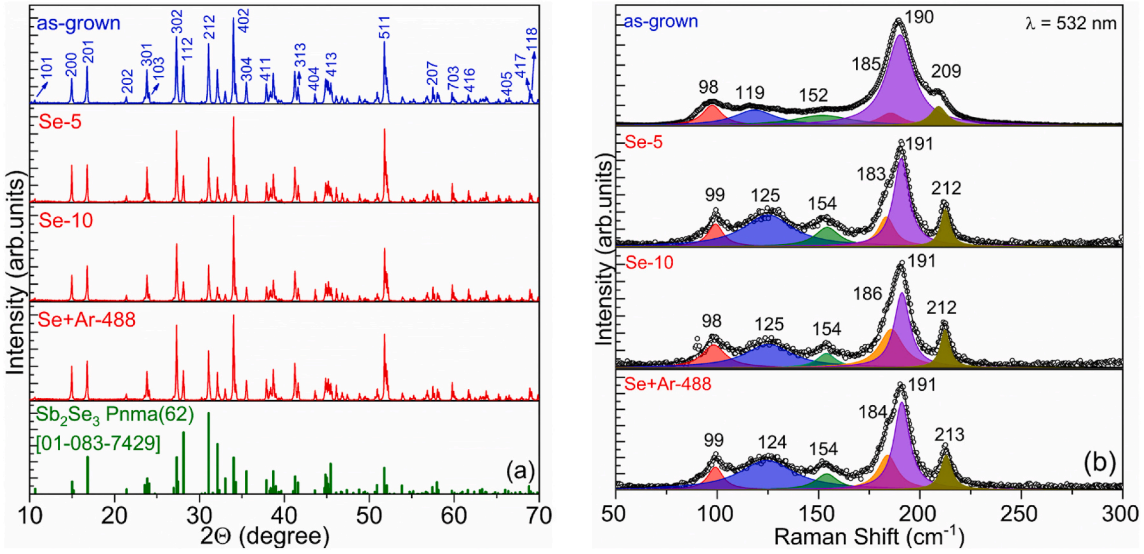

Fig. 3. (a) The XRD patterns and the simulated pattern according to the Pnma(62) space group. (b) Room-temperature Raman spectra of the as-grown, Se-5, Se-10, and Se + Ar-488 Sb_2Se_3 polycrystals. Solid black lines represent fitted curves using Lorentzian functions, and experimental data are shown as scatter points.

sizes were determined from the diffraction patterns using the Halder–Wagner method (see Experimental section), and the Raman A_{g2} mode linewidths were obtained from Lorentzian fitting; the resulting values are summarized in Table 2. All post-treated samples exhibit larger crystallite sizes than the as-grown material, and the lattice strain is zero in all samples. The Raman linewidth is reduced by almost a factor of two after selenization, which might indicate a substantial reduction of local structural disorder. Since no additional Sb–Se phases are observed, these structural improvements occur within the orthorhombic Sb_2Se_3 phase. The differences among the post-treated samples are, however, small, and the distinction between the effects of the different selenization conditions is provided by the photoluminescence analysis presented in Section 3.2.

Room-temperature Raman spectra of the as-grown and post-treated Sb_2Se_3 polycrystals (Fig. 3b) exhibit characteristic vibrational modes of orthorhombic Sb_2Se_3, with prominent peaks located at approximately 155, 190, and 210 cm^{-1}, consistent with reported A_g symmetry modes [32–34]. The Raman spectra confirm the single-phase Sb_2Se_3 composition of both as-grown and post-treated polycrystals, while the dominating A_g^2 mode exhibits a slight shift toward higher wavenumbers after thermal treatments. Furthermore, post-annealing, particularly in Se + Ar-488 polycrystals, leads to a reduction in the FWHM of the main Raman peaks, indicating improved crystallinity and reduced structural disorder, which is consistent with the findings from previous selenization studies [17].

Since no detectable bulk structural changes were observed, the variations in the following optical response are attributed to modifications in intrinsic defect-related recombination processes.

3.2. Photoluminescence results

Fig. 4a illustrates the low-temperature (T = 8 K) PL spectra of the as-grown and post-treated Sb_2Se_3 samples (Se-5, Se-10, and Se + Ar-488). The sharp, narrow features observed at ~0.9 eV are attributed to atmospheric water vapor absorption and do not correspond to intrinsic Sb_2Se_3 emission.

To quantitatively resolve the low-temperature (T = 8 K) emission features, each spectrum was deconvoluted using an asymmetric double-sigmoidal (ADS) function (Fig. 4a) [35].

$$I(E) = A\left(1 \Big/ 1 + exp\left(-\frac{E - E_{max} + W_{peak}/2}{W_{low}}\right)\right) \cdot \left(1 - 1 \Big/ 1 + exp\left(-\frac{E - E_{max} + W_{peak}/2}{W_{high}}\right)\right) \quad (1)$$

where A is the amplitude, E_{max} is a parameter related to the peak position, and Wlow and Whigh describe the low- and high-energy slope widths from the low- and high-energy side of the peak, respectively. These parameters define the asymmetric shape of the emission band and do not directly correspond to the physical peak energy or full width at half maximum (FWHM). The actual PL peak energies used in subsequent analyses were determined numerically from the fitted curve maxima. The apparent asymmetry of the PL4 band, with a seemingly extended low-energy side, is predominantly instrumental: the high-energy wing of the band is attenuated by the steeply decreasing responsivity of the InGaAs detector near its short-wavelength cutoff. Since this attenuation is identical for all samples and temperatures, the comparative analysis of the PL4 intensity, linewidth, and peak position remains unaffected.

Table 2
Average crystallite size of the orthorhombic Sb_2Se_3 phase obtained from the Halder–Wagner analysis of the diffraction patterns, and FWHM of the Raman A_{g2} mode obtained from Lorentzian fitting, for the as-grown and post-treated samples.

Sample name	Crystallite size (Å)	Raman FWHM (cm^{-1}) at ~ 190 cm^{-1}
as-grown	499 ± 17	13.8 ± 0.7
Se-5	607 ± 31	9.3 ± 0.3
Se-10	623 ± 33	7.9 ± 1.7
Se + Ar-488	545 ± 12	8.7 ± 0.5

The fitting procedure of the as-grown spectra resolves four distinct emission bands located at 0.88 eV (PL1), 1.10 eV (PL2), 1.22 eV (PL3), and 1.29 eV (PL4), as shown in Fig. 4a. In contrast, the post-treated samples exhibit only two dominant contributions at 0.88 eV (PL1) and ~1.30 eV (PL4), indicating a pronounced suppression of the PL2 and PL3 bands upon selenization. PL2 and PL3 bands were also reported by Grossberg et al. [26] and attributed to grain-boundary-related and DAP recombination, respectively. In addition to the elimination of these defect-related bands, increasing vapor pressure leads to a substantial modification of the band-edge emission, manifested as a progressive increase in its relative intensity accompanied by a clear narrowing of its linewidth, from 56.3 meV for the as-grown sample to 45.7 meV for the Se + Ar-488 sample. This effect is most pronounced for the Se + Ar-488 polycrystals, where PL4 exhibits the highest intensity and the narrowest linewidth among all samples.

Fig. 4b confirms the trends observed in Fig. 4a and further reveals the combined effect of selenization and argon atmosphere on defect-related emission, in which all spectra are normalized to the intensity of the band-edge emission (PL4 at ~1.30 eV). Notably, the sample annealed only under argon (200 Torr) already shows suppression of the PL2 band, indicating that the argon atmosphere alone suppresses the grain-boundary-related band. In contrast, the combined selenization and argon treatment (Se + Ar-488) leads to suppression of both PL2 and PL3 bands together with a significant reduction of the PL1 emission. This normalization allows evaluation of relative changes in deep-level recombination independent of overall emission intensity, which is most pronounced for the Se + Ar-488 sample.

To further elucidate the recombination mechanisms and assess the thermal stability of the emission channels, temperature-dependent PL measurements were performed between 8 K and 300 K (Fig. 5a). The evolution of the spectra confirms the conclusions drawn from the low-temperature (T = 8 K) PL analysis. With increasing temperature, all samples exhibit progressive thermal quenching of the integrated PL intensity; however, the quenching behavior differs significantly between PL1 and PL4. The deep-level emission (PL1) shows a rapid reduction in intensity, whereas the excitonic emission (PL4) remains comparatively more thermally robust. This contrast indicates that PL1 is strongly influenced by defect-related recombination channels. Notably, the Se + Ar-488 sample maintains the highest relative PL4 intensity over the entire temperature range, suggesting reduced thermally activated recombination compared to the other samples. The enhanced thermal stability of PL4 is consistent with the reduced peak width and increased relative intensity observed at T = 8 K, supporting the interpretation of improved electronic uniformity and reduced defect density.

The temperature dependence of the PL peak energies (E_{max}), determined from the maxima of the fitted ADS curves, provides further insight into the origin of the emission bands and the effect of vapor pressure during selenization (Fig. 5b). For the as-grown polycrystals, the four resolved emission bands exhibit distinctly different temperature dependences. PL1 shows only weak temperature dependence, with a relatively small energy shift over the investigated temperature range, consistent with its deep-level character. PL2 exhibits a slight temperature-induced redshift comparable to the band gap variation. Grossberg et al. [26] reported a similar sub-band gap transition and, considering its position relative to the low-temperature band gap of Sb_2Se_3 (E_g = 1.32 eV) [26,36], attributed it to recombination processes associated with defect levels at grain boundaries. PL3 was also identified by Grossberg et al. [26] who reported a similar emission at ~1.24 eV and attributed it to donor–acceptor pair (DAP) recombination. The deviation

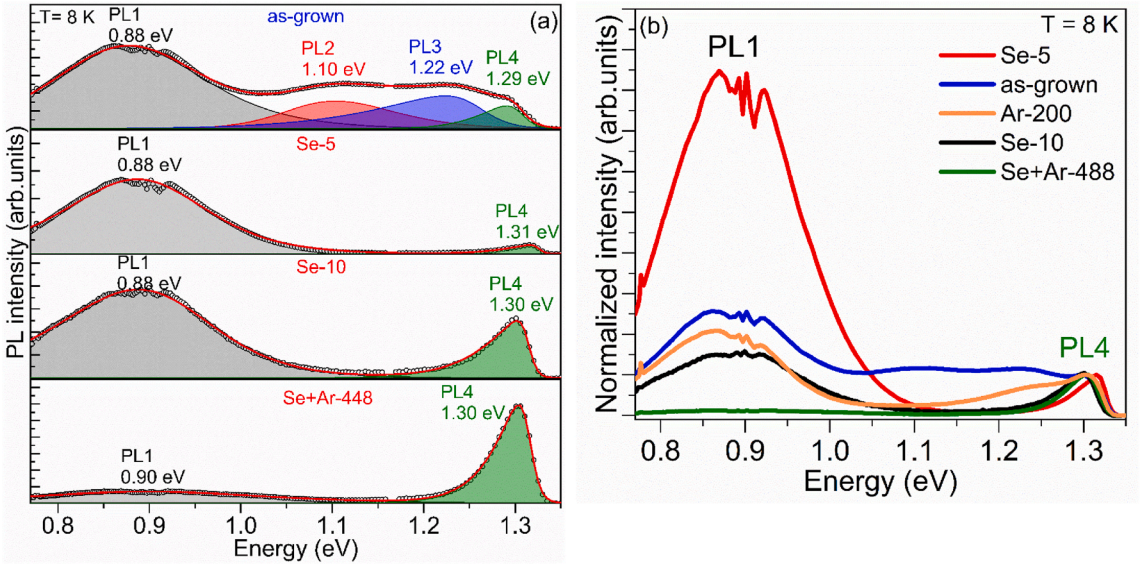

Fig. 4. (a) Low-temperature (T = 8 K) PL spectra of as-grown, Se-5, Se-10, and Se + Ar-488 Sb_2Se_3 polycrystals. The experimental data are presented as black scatter points, while the fitted PL bands using an asymmetric double-sigmoidal (ADS) function are shown as solid lines. (b) Direct comparison of low-temperature (T = 8 K) PL spectra normalized to the intensity of the band-edge emission (PL4 at ~ 1.30 eV), highlighting the relative suppression of deep-defect bands (PL1, PL2, PL3) upon selenization.

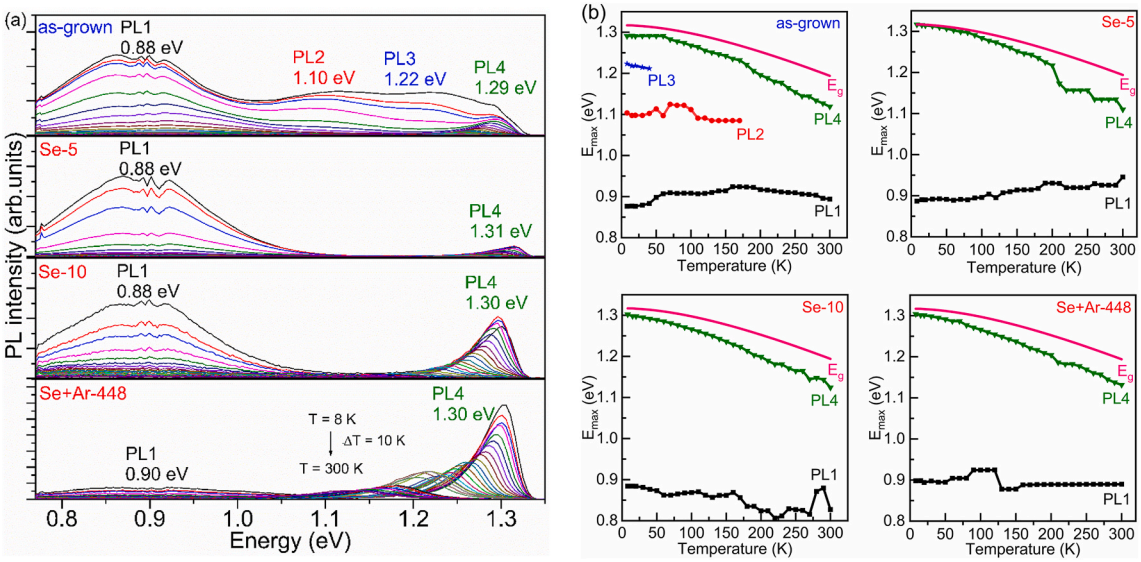

Fig. 5. (a) Temperature-dependent PL spectra of as-grown, Se-5, Se-10, and Se + Ar-488 Sb_2Se_3 polycrystals measured at an excitation power density of 1500 mW/cm2. (b) Temperature dependence of the PL peak positions (E_{max}) together with the temperature-dependent band gap $E_g(T)$ described by the Varshni expression [29].

of PL3 from ideal band gap tracking and its thermally activated behavior, as well as a small blueshift on the order of a few meV/decade of laser power observed here, are consistent with a DAP mechanism. The high-energy PL4 band exhibits a systematic redshift with increasing temperature that closely follows the expected band gap shrinkage behavior, characteristic of band-edge emission. This observation is consistent with previous reports by Krustok et al. [25], where a similar emission was attributed to excitonic recombination.

In the post-treated polycrystals, PL4 follows the Varshni-type band gap trend [37] more closely than in the as-grown material. This effect is particularly pronounced for the Se + Ar-488 sample, where PL4 exhibits a smooth and monotonic redshift consistent with temperature. The improved agreement with band gap evolution indicates reduced influence of defect-related recombination and a more pronounced excitonic contribution. Conversely, PL1 in all samples retains weak temperature dispersion and a clear deviation from $E_g(T)$, confirming its deep-level origin and localized character. Given its position and strong thermal quenching, it is most consistent with recombination involving localized deep defects, potentially arising from deep donor-deep acceptor pair recombination as was detected previously in Sb_2Se_3 polycrystals for the PL band at a similar position of 0.94 eV [26].

The thermal activation energies were determined by the Arrhenius plot (Fig. 6) from the temperature dependencies of the integrated intensities of the PL bands [38]:

$$\varnothing(T) = \varnothing_0 \Big/ \left[1 + \alpha \exp\left(-E_a/_{KT}\right)\right] \quad (2)$$

Where Φ is the integrated intensity, α is the process rate parameter, and E_a is the thermal activation energy. To ensure reliable extraction of activation energies, the fitting was restricted to the temperature interval

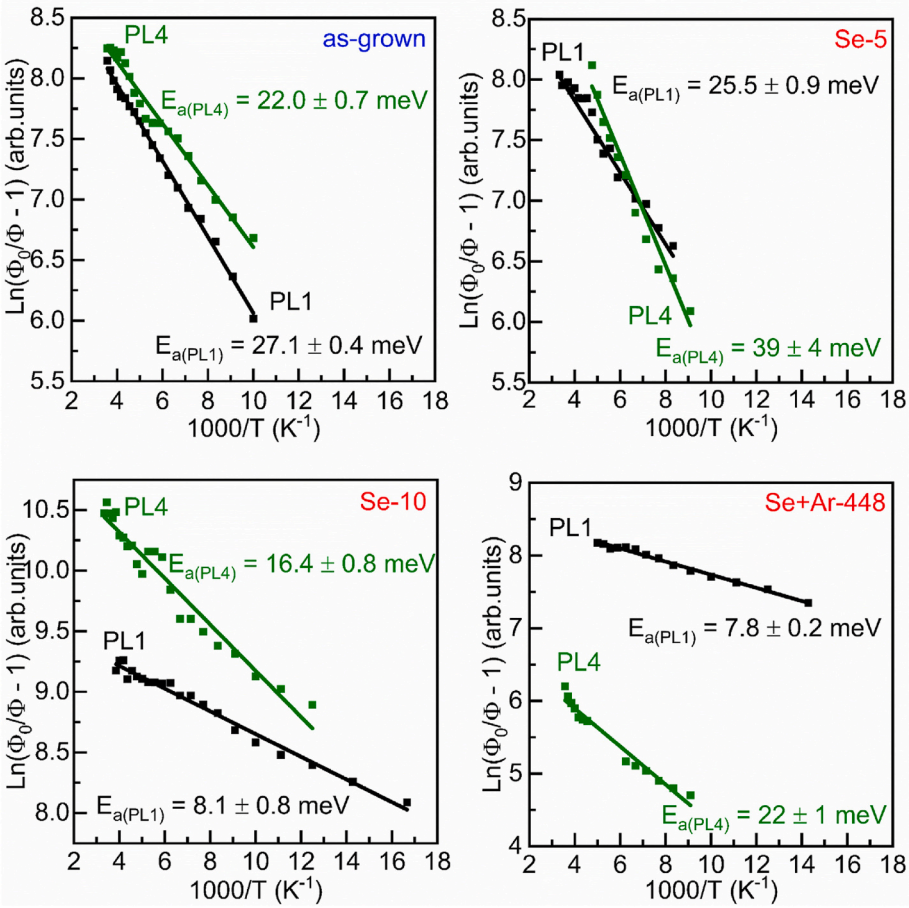

Fig. 6. Arrhenius plots were used to determine the thermal activation energies for the PL bands in as-grown, Se-5, Se-10, and Se + Ar-488 Sb_2Se_3 polycrystals.

where the quenching behavior exhibited a clear Arrhenius-type linear dependence in $\ln(\Phi_0/\Phi - 1)$ versus $1000/T$ plots. The low-temperature regime, where the emission intensity remains nearly constant, was excluded from the fitting procedure, as it does not contribute to the thermally activated component of the recombination dynamics. The Arrhenius analysis was restricted to the emission bands for which reliable temperature-dependent integrated intensities could be extracted over a sufficiently broad thermally activated regime. For the PL2 and PL3 bands, their rapid thermal quenching resulted in a limited number of reliable data points, preventing robust extraction of activation energies. Consequently, no Arrhenius parameters are reported for these bands. The extracted activation energies for PL1 and PL4 remain within the same order of magnitude across all samples, being in the range from 16 meV to 40 meV for PL4 and in the range from 8 meV to 27 meV for PL1. Extremely small thermal activation energies were obtained for PL1, considering the large distance of the PL1 band from the band gap energy, further confirming the possible origin of this PL band from deep donor – deep acceptor pair recombination as was observed in Ref. [26]. It must be highlighted that although a similar deep PL band around 0.9 eV has been detected in Sb_2Se_3 in different studies [26,27], the involved deep defects seem to vary from sample to sample, as reflected in varying thermal activation energies of the deep PL band (93 meV in Ref. [26] and 5 meV in Ref. [27]). In contrast, in Cl-doped Sb_2Se_3, a deep PL emission at 0.84 eV was influenced by dopant-induced defect states, resulting in a different recombination behavior compared to the undoped material [27]. In the case of Cl-doped Sb_2Se_3, a PL band at 0.84 eV was assigned to band-bending influenced donor-acceptor pair recombination involving a deep acceptor with an ionization energy of 152 ± 6 meV and a Cl-induced shallow donor. This indicates that the deep PL in Sb_2Se_3 can also be modified by extrinsic dopants. Notably, no significant variation in thermal activation energy is observed with increasing vapor pressure during selenization. Instead, the primary effect of post-treatment is the modification of the relative contributions of existing recombination pathways, particularly the suppression of deep-level bands PL1, PL2, and PL3 and the enhancement of the excitonic PL4 emission. These observations indicate that the applied thermal post-treatments do not introduce new recombination mechanisms in Sb_2Se_3, but rather modify the density of defect-related states and enhance the excitonic radiative recombination.

To further elucidate the recombination mechanisms corresponding to detected PL bands, excitation power-dependent PL measurements were performed at T = 8 K (Fig. 7a). As the excitation power increases, the overall emission intensity increases for all samples, with no emergence of new emission bands. The dominant contributions remain associated with PL1 and PL4 in post-treated samples, consistent with the suppression of PL2 and PL3 defect-related recombination channels.

The integrated PL intensity Φ of each emission band was analyzed as a function of excitation power P using the power-law relation, $\Phi \sim P^k$, where the power coefficient (k) can be obtained from the slope of the $\Phi(P)$ dependence on a log-log scale. In the as-grown polycrystal (Fig. 7b), PL1 exhibits sublinear behavior ($k = 0.6$), while PL2 and PL3 show similar sublinear exponents ($k = 0.7$), indicating recombination of charge carriers localized at defect states within the band gap [39]. In contrast, the PL4 band demonstrates a slightly superlinear dependence ($k = 1.2$), indicative of excitonic recombination. This behavior is consistent with its band-edge origin, further supported by its

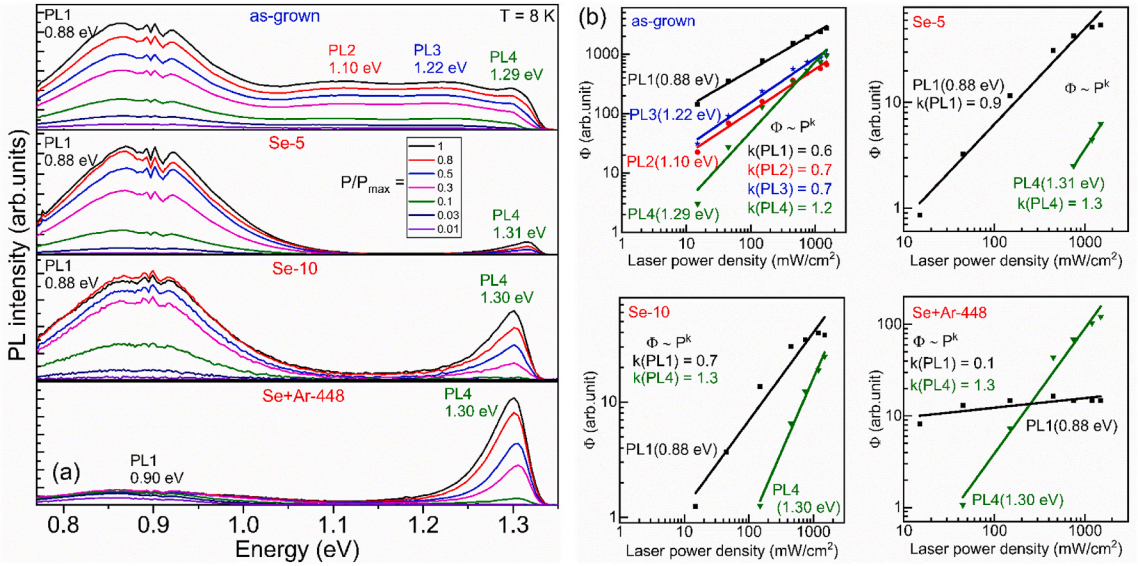

Fig. 7. (a) Laser power-dependent PL spectra of as-grown, Se-5, Se-10, and Se + Ar-488 Sb_2Se_3 polycrystals measured at T = 8 K. (b) Excitation power dependence of the integrated PL intensity (Φ) on a log–log scale. Solid lines represent linear fits.

temperature dependence following the band gap variation, in agreement with previous reports by Krustok et al. [25]. In the post-treated samples, only PL1 and PL4 contributions are observed, showing the same behaviour as in the as-grown sample. These results further support the distinction between defect-related and excitonic recombination channels, as reflected in the sublinear and superlinear power dependencies of PL1 and PL4, respectively.

After post-treatment, PL1 exhibited excitation-induced peak shifts in the range of 3–10 meV per decade, which could be considered typical also for conventional donor–acceptor pair recombination [40]. However, considering the very deep spectral position of the PL1 band together with its small thermal activation energies, this band can be explained by the deep donor–deep acceptor pair recombination model [26,40]. In contrast, PL3 shifts by only a few meV per decade, consistent with conventional donor–acceptor pair recombination.

Assignment of the observed PL bands to specific defect species is not trivial, one can propose possible defects based on the DFT calculations considering the stoichiometry of the synthesized material. Based on energy balance analysis and comparison with published defect characterization studies of Sb_2Se_3. The recombination energy of PL1 constrains the participating defect levels through the energy balance [41]:

$$h\nu_{max} = E_g - (E_d + E_a) + \frac{e^2}{4\pi\varepsilon_0\varepsilon r} \quad (3)$$

where E_g is the band gap energy, E_d and E_a are the donor and acceptor ionization energies, respectively. While in the term representing the Coulomb interaction between the donor and acceptor, e is the electron charge, ε_0 is the permittivity of vacuum, ε is statistic dielectric constant, and r is the donor-acceptor pair distance. Assuming nearest-neighbour donor–acceptor pairs with r = 0.2588 nm, corresponding to the shortest Sb(2)–Se(1) distance in the Sb_2Se_3 crystal structure [42], and ε = 24 [43], the Coulomb term amounts to $E_C \approx 0.232$ eV. With E_g(8 K) ≈ 1.32 eV [36,44] and hν (PL1) = 0.88 eV, the sum of the donor and acceptor ionization energies could then be $E_d + E_a \approx 0.67$ eV. One possible combination satisfying this balance involves the V_{Se2} deep donor, reported at ~0.3 eV below the conduction band [6] and detected by DLTS with activation energies of 0.36–0.39 eV [11,13], paired with a deep acceptor with an ionization energy of roughly 0.3 eV. The persistence of PL1 in all samples might then reflect the reported stability of V_{Se2} under Se-rich conditions, where its formation energy is predicted to be almost negative, much smaller than those of V_{Se1} and V_{Se3} [6].

PL3 is likely related to shallow DAP recombination involving the Se_{Sb1} antisite acceptor, following the assignment of Grossberg et al. [26]. Its rapid suppression upon selenization suggests the elimination of the shallow donor partners, consistent with the predicted destabilization of donor defects with increasing Se chemical potential [11]. PL2 has been associated with recombination at grain boundaries [26]; its suppression already after annealing in an inert atmosphere might indicate passivation of grain boundaries, with further improvement under selenization. PL4 is excitonic band-edge emission [25], and its increased intensity and reduced linewidth reflect the improved crystal quality of the selenized samples.

The strong suppression of the deep-defect emission and the narrowing of the excitonic linewidth in the Se + Ar-488 sample imply an enhanced external radiative efficiency of the absorber, which potentially reduces the recombination-related V_{OC} loss [6,13,14]. These results identify the vapor pressure during selenization as a practical processing parameter for improving the optoelectronic quality of Sb_2Se_3 absorbers.

4. Conclusion

In this work, Sb_2Se_3 polycrystals were subjected to post-growth selenization under controlled vapor pressure conditions, and the resulting changes in defect-related recombination were studied by temperature- and excitation-power-dependent photoluminescence spectroscopy. Four emission bands were resolved in the as-grown material and attributed to deep donor-deep acceptor (PL1), grain-boundary-related (PL2), donor-acceptor pair (PL3), and excitonic (PL4) recombination. Based on energy balance analysis and comparison with reported defect characterization studies, PL1 is attributed to recombination involving the V_{Se2} deep donor, while PL3 is associated with DAP recombination involving the Se_{Sb1} antisite acceptor.

Selenization suppresses the PL2 and PL3 bands and progressively reduces the deep-level PL1 emission with increasing vapor pressure, while the excitonic PL4 emission becomes dominant, exhibiting enhanced intensity and reduced linewidth. The persistence of PL1 in all samples is consistent with first-principles predictions that the V_{Se2} vacancy remains thermodynamically stable even under Se-rich conditions. These results show that increasing the vapor pressure during

selenization not only does not introduce new recombination mechanisms, but also reduces the density of defect-related states and promotes excitonic radiative recombination, argon-assisted high-pressure selenization (Se + Ar-488) being the most effective. The vapor pressure during selenization is thus identified as a key parameter for controlling deep-defect-mediated recombination in Sb_2Se_3, providing a practical processing route toward improved absorber quality.

CRediT authorship contribution statement

N. Abbasi: Conceptualization, Data curation, Methodology, Visualization, Writing – original draft, Writing – review & editing. **J. Krustok:** Conceptualization, Writing – review & editing. **R. Kaupmees:** Methodology, Writing – review & editing. **K. Timmo:** Methodology, Writing – review & editing. **V. Mikli:** Methodology. **M. Kauk-Kuusik:** Conceptualization, Writing – review & editing. **M. Grossberg-Kuusk:** Conceptualization, Funding acquisition, Project administration, Supervision, Writing – review & editing.

Declaration of competing interests

The authors declare that they have no known competing financial interests or personal relationships that could have appeared to influence the work reported in this paper.

Acknowledgements

This work was supported by the Estonian Research Council [grant number PRG1023]; ERA.net" title = "http://M-ERA.net">M-ERA.net project LightCell [grant number MNHA23040]; ERDF project GREENTECH [grant number TK210], and CETP project SUNLIFE [grant number Cetp-FP-2023–00137].

Data availability

Data will be made available on request.

References

[1] O. Poncelet, R. Kotipalli, B. Vermang, A. Macleod, L.A. Francis, D. Flandre, Optimisation of rear reflectance in ultra-thin CIGS solar cells towards >20% efficiency, Sol. Energy 146 (2017) 443–452, https://doi.org/10.1016/j.solener.2017.03.001.

[2] Y. Zhou, L. Wang, S. Chen, S. Qin, X. Liu, J. Chen, D.-J. Xue, M. Luo, Y. Cao, Y. Cheng, E.H. Sargent, J. Tang, Thin-film Sb_2Se_3 photovoltaics with oriented one-dimensional ribbons and benign grain boundaries, Nat. Photonics 9 (2015) 409–415, https://doi.org/10.1038/nphoton.2015.78.

[3] H. Guo, B. Shen, X. Wang, J. Xiao, W. Deng, S. Jiang, L. Xu, X. Dong, L. Li, S. Zhang, J. Qiu, N. Yuan, J. Ding, Active selenium-driven confined crystallization and carrier dynamics in high-efficiency ultrathin semi-transparent Sb_2Se_3 solar cells, Chem. Sci. 17 (2026) 4753–4764, https://doi.org/10.1039/d5sc08223d.

[4] N. Cifuentes, S. Ghosh, A. Shongolova, M.R. Correia, P.M.P. Salomé, P. A. Fernandes, S. Ranjbar, S. Garud, B. Vermang, G.M. Ribeiro, J.C. González, Electronic conduction mechanisms and defects in polycrystalline antimony selenide, J. Phys. Chem. C 124 (2020) 7677–7682, https://doi.org/10.1021/acs.jpcc.0c00398.

[5] X. Wen, C. Chen, S. Lu, K. Li, R. Kondrotas, Y. Zhao, W. Chen, L. Gao, C. Wang, J. Zhang, G. Niu, J. Tang, Vapor transport deposition of antimony selenide thin film solar cells with 7.6% efficiency, Nat. Commun. 9 (2018) 2179, https://doi.org/10.1038/s41467-018-04634-6.

[6] S. Dong, G. Li, J. Hong, R. Qi, S. Yang, P. Yang, L. Sun, F. Yue, Deep defects limiting the conversion efficiency of Sb_2Se_3 thin-film solar cells, Phys. Chem. Chem. Phys. 25 (2023) 4617–4623, https://doi.org/10.1039/d2cp05585f.

[7] L. Grad, F.V. Rohr, J. Zhao, M. Hengsberger, J. Osterwalder, Photoexcited charge carrier dynamics in Sb_2Se_3(100), Phys. Rev. Mater. 4 (10) (2020) 105404. Oct 26; 4, https://doir.org/10.1103/PhysRevMaterials.4.105404.

[8] W. Yang, S. Lee, H.C. Kwon, J. Tan, H. Lee, J. Park, Y. Oh, H. Choi, J. Moon, Time-resolved observations of photo-generated charge-carrier dynamics in Sb_2Se_3 photocathodes for photoelectrochemical water splitting, ACS Nano 12 (2018) 11088–11097, https://doi.org/10.1021/acsnano.8b05446.

[9] R. Cao, H. Cai, W. Lian, R. Tang, Y. Xiang, Y. Wang, T. Chen, Revealing the chemical structure-dependent carrier trapping in one-dimensional antimony selenide photovoltaic materials, J. Mater. Chem. A 10 (2022) 20482–20488, https://doi.org/10.1039/d2ta03044f.

[10] Y. Zhao, S. Wang, C. Li, B. Che, X. Chen, H. Chen, R. Tang, X. Wang, G. Chen, T. Wang, J. Gong, T. Chen, X. Xiao, J. Li, Regulating deposition kinetics via a novel additive-assisted chemical bath deposition technology enables fabrication of 10.57%-efficiency Sb_2Se_3 solar cells, Energy Environ. Sci. 15 (2022) 5118–5128, https://doi.org/10.1039/d2ee02261c.

[11] U. Wijesinghe, G. Longo, O.S. Hutter, Defect engineering in antimony selenide thin film solar cells, Energy Adv. 2 (2023) 12–33, https://doi.org/10.1039/d2ya00232a.

[12] X. Wang, H. Zhang, H. Xia, Y. Guo, P. Hu, J. Li, Pathways toward efficient antimony chalcogenide solar cells: material development, film engineering, defect passivation, and carrier transport, Adv. Funct. Mater. 36 (2026) e23084, https://doi.org/10.1002/adfm.202523084.

[13] T.D.C. Hobson, L.J. Phillips, O.S. Hutter, K. Durose, J.D. Major, Defect properties of Sb_2Se_3 thin film solar cells and bulk crystals, Appl. Phys. Lett. 116 (2020) 261101, https://doi.org/10.1063/5.0012697.

[14] W. Lian, R. Cao, G. Li, H. Cai, Z. Cai, R. Tang, C. Zhu, S. Yang, T. Chen, Distinctive deep-level defects in non-stoichiometric Sb_2Se_3 photovoltaic materials, Adv. Sci. 9 (2022) 2105268, https://doi.org/10.1002/advs.202105268.

[15] E. Cho, S.J. Sung, K.J. Yang, J. Lee, V.Q. Hoang, B. Kadiri-English, D.K. Hwang, J. K. Kang, D.H. Kim, Enhanced p-type conductivity in Sb_2Se_3 through alkali and alkaline earth metal doping, J. Mater. Chem. A 13 (2025) 8507–8517, https://doi.org/10.1039/d4ta08978b.

[16] M. Leng, M. Luo, C. Chen, S. Qin, J. Chen, J. Zhong, J. Tang, Selenization of Sb_2Se_3 absorber layer: an efficient step to improve device performance of CdS/Sb_2Se_3 solar cells, Appl. Phys. Lett. 105 (2014) 083905, https://doi.org/10.1063/1.4894170.

[17] V. Kumar, E. Artegiani, P. Punathil, M. Bertoncello, M. Meneghini, F. Piccinelli, A. Romeo, Analysis of Se co-evaporation and post-selenization for Sb_2Se_3-based solar cells, ACS Appl. Energy Mater. 4 (2021) 12479–12486, https://doi.org/10.1021/acsaem.1c02301.

[18] G.X. Liang, Y.D. Luo, S. Chen, R. Tang, Z.H. Zheng, X.J. Li, X.S. Liu, Y.K. Liu, Y. F. Li, X.Y. Chen, Z.H. Su, X.H. Zhang, H.L. Ma, P. Fan, Sputtered and selenized Sb_2Se_3 thin-film solar cells with open-circuit voltage exceeding 500 mV, Nano Energy 73 (2020) 104806, https://doi.org/10.1016/j.nanoen.2020.104806.

[19] Q. Zhao, B. Che, H. Wang, X. Peng, J. Yang, R. Tang, C. Zhu, T. Chen, Crystal reconstruction and defect healing enabled high-quality Sb_2Se_3 films for solar cell applications, J. Mater. Chem. A 12 (2024) 11524–11534, https://doi.org/10.1039/d4ta00734d.

[20] T.P. Weiss, I. Minguez-Bacho, E. Zuccalà, M. Melchiorre, N. Valle, B. El Adib, T. Yokosawa, E. Spiecker, J. Bachmann, P.J. Dale, S. Siebentritt, Post-deposition annealing and interfacial atomic layer deposition buffer layers of Sb_2Se_3/CdS stacks for reduced interface recombination and increased open-circuit voltages, Prog. Photovoltaics Res. Appl. 31 (2023) 203–219, https://doi.org/10.1002/pip.3625.

[21] S. Rijal, D.B. Li, R.A. Awni, S.S. Bista, Z. Song, Y. Yan, Influence of post-selenization temperature on the performance of substrate-type Sb_2Se_3 solar cells, ACS Appl. Energy Mater. 4 (2021) 4313–4318, https://doi.org/10.1021/acsaem.1c00657.

[22] H. He, Y. Zhong, W. Zou, X. Zhang, J. Zhao, M. Ishaq, G. Liang, A novel Se-diffused selenization strategy to suppress bulk and interfacial defects in Sb_2Se_3 thin film solar cell, Surf. Interfaces 51 (2024) 104793, https://doi.org/10.1016/j.surfin.2024.104793.

[23] R. Tang, X.Y. Chen, G.X. Liang, Z.H. Su, J.T. Luo, P. Fan, Magnetron sputtering deposition and selenization of Sb_2Se_3 thin film for substrate Sb_2Se_3/CdS solar cells, Surf. Coat. Technol. 360 (2019) 68–72, https://doi.org/10.1016/j.surfcoat.2018.12.102.

[24] M.E. Uslu, K. Muska, M. Pilvet, S. Bereznev, V. Mikli, M. Kauk-Kuusik, M. Grossberg-Kuusk, Enhanced grain orientation in Sb_2Se_3 thin films deposited on Mo/BSG substrates via RF-sputtering and selenization, Mater. Sci. Semicond. Process. 184 (2024) 108835, https://doi.org/10.1016/j.mssp.2024.108835.

[25] J. Krustok, R. Kondrotas, R. Nedzinskas, K. Timmo, R. Kaupmees, V. Mikli, M. Grossberg, Identification of excitons and biexcitons in Sb_2Se_3 under high photoluminescence excitation density, Adv. Opt. Mater. 9 (2021) 2100107, https://doi.org/10.1002/adom.202100107.

[26] M. Grossberg, O. Volobujeva, A. Penežko, R. Kaupmees, T. Raadik, J. Krustok, Origin of photoluminescence from antimony selenide, J. Alloys Compd. 817 (2020) 152716, https://doi.org/10.1016/j.jallcom.2019.152716.

[27] N. Abbasi, J. Krustok, R. Kaupmees, M. Danilson, T.D.C. Hobson, J.D. Major, K. Durose, M. Kauk-Kuusik, M. Grossberg-Kuusk, Study of defects in chlorine-doped Sb_2Se_3 single crystals by photoluminescence spectroscopy, J. Alloys Compd. Commun. 10 (2026) 100171, https://doi.org/10.1016/j.jacomc.2026.100171.

[28] G. Ghosh, The Sb-Se (antimony-selenium) system, J. Phase Equil. 14 (1993) 753–763, https://doi.org/10.1007/BF02667889.

[29] Z.S. Aliev, S.S. Musaeva, D.M. Babanly, A.V. Shevelkov, M.B. Babanly, Phase diagram of the Sb-Se-I system and thermodynamic properties of SbSeI, J. Alloys Compd. 505 (2010) 450–455, https://doi.org/10.1016/j.jallcom.2010.06.103.

[30] O.C. Olatunde, R. Marzouki, A. Brahmia, D.C. Onwudiwe, Lattice strain analysis of antimony sulphide nanorods, J. Clust. Sci. 34 (2023) 2017–2027, https://doi.org/10.1007/s10876-022-02363-x.

[31] M.E. Uslu, M. Danilson, K. Timmo, M. Grossberg-Kuusk, The effect of tin doping on the band structure and optical properties of polycrystalline antimony selenide, Physica B 678 (2024) 415744, https://doi.org/10.1016/j.physb.2024.415744.

[32] N. Fleck, T.D.C. Hobson, C.N. Savory, J. Buckeridge, T.D. Veal, M.R. Correia, D. O. Scanlon, K. Durose, F. Jäckel, Identifying Raman modes of Sb_2Se_3 and their symmetries using angle-resolved polarised Raman spectra, J. Mater. Chem. A 8 (2020) 8337–8344, https://doi.org/10.1039/d0ta01783c.

[33] P. Vidal-Fuentes, M. Guc, X. Alcobe, T. Jawhari, M. Placidi, A. Pérez-Rodríguez, E. Saucedo, V. Izquierdo-Roca, Multiwavelength excitation Raman scattering study of Sb_2Se_3 compound: fundamental vibrational properties and secondary phases detection, 2D Mater. 6 (2019) 045054, https://doi.org/10.1088/2053-1583/ab4029.

[34] A. Shongalova, M.R. Correia, B. Vermang, J.M.V. Cunha, P.M.P. Salomé, P. A. Fernandes, On the identification of Sb_2Se_3 using Raman scattering, MRS Commun. 8 (2018) 865–870, https://doi.org/10.1557/mrc.2018.94.

[35] J. Krustok, H. Collan, M. Yakushev, K. Hjelt, The role of spatial potential fluctuations in the shape of the PL bands of multinary semiconductor compounds, Phys. Scripta T79 (1999) 179–182, https://doi.org/10.1088/0031-8949/1999/T79/179.

[36] Y.P. Varshni, Temperature dependence of the energy gap in semiconductors, Physica 34 (1967) 149–154, https://doi.org/10.1016/0031-8914(67)90062-6.

[37] M. Birkett, W.M. Linhart, J. Stoner, L.J. Phillips, K. Durose, J. Alaria, J.D. Major, R. Kudrawiec, T.D. Veal, Band gap temperature-dependence of close-space sublimation grown Sb_2Se_3 by photo-reflectance, APL Mater. 6 (2018) 084901, https://doi.org/10.1063/1.5027157.

[38] J. Krustok, H. Collan, K. Hjelt, Does the low-temperature Arrhenius plot of the photoluminescence intensity in CdTe point towards an erroneous activation energy? J. Appl. Phys. 81 (1997) 1442–1445, https://doi.org/10.1063/1.364955.

[39] T. Schmidt, K. Lischka, W. Zulehner, Excitation-power dependence of the near-band-edge photoluminescence of semiconductors, Phys. Rev. B 45 (1992) 8989–8994, https://doi.org/10.1103/PhysRevB.45.8989.

[40] A.P. Levanyuk, V.V. Osipov, Edge luminescence of direct-gap semiconductors, Sov. Phys. Usp. 24 (1981) 187–215, https://doi.org/10.1070/PU1981v024n03ABEH004770.

[41] F. Williams, Donor-acceptor pairs in semiconductors, Phys. Status Solidi 25 (1968) 493–512, https://doi.org/10.1002/pssb.19680250202.

[42] V.L. Deringer, R.P. Stoffel, M. Wuttig, R. Dronskowski, Vibrational properties and bonding nature of Sb_2Se_3 and their implications for chalcogenide material, Chem. Sci. 6 (2015) 5255–5262, https://doi.org/10.1039/c5sc00825e.

[43] C. Chen, D.C. Bobela, Y. Yang, S. Lu, K. Zeng, C. Ge, B. Yang, L. Gao, Y. Zhao, M. C. Beard, J. Tang, Characterization of basic physical properties of Sb_2Se_3 and its relevance for photovoltaics, Front. Optoelectron. 10 (2017) 18–30, https://doi.org/10.1007/s12200-017-0702-z.

[44] C. Chen, W. Li, Y. Zhou, C. Chen, M. Luo, X. Liu, K. Zeng, B. Yang, C. Zhang, J. Han, J. Tang, Optical properties of amorphous and polycrystalline Sb_2Se_3 thin films prepared by thermal evaporation, Appl. Phys. Lett. 107 (2015) 043905, https://doi.org/10.1063/1.4927741.